Chaos, Solitons and Fractals 104 (2017) 18–27

Contents lists available at ScienceDirect

Chaos, Solitons and Fractals

Nonlinear Science, and Nonequilibrium and Complex Phenomena

journal homepage: www.elsevier.com/locate/chaos

Frontiers

Dynamics of a pendulum driven by a DC motor and magnetically controlled

B. Nana [a,*], S.B. Yamgoué [a], R. Tchitnga [b], P. Woafo [c]

[a] Department of Physics, Higher Teacher Training College, University of Bamenda, PO Box 39 Bamenda, Cameroon
[b] Laboratory of Electronics and Signal Processing, Faculty of Science, University of Dschang, PO Box 67 Dschang, Cameroon
[c] Laboratory of Modelling and Simulation in Engineering, Biomimetics and Prototypes, Faculty of Science, University of Yaounde I, PO Box 812 Yaounde, Cameroon

ARTICLE INFO

Article history:
Received 2 January 2017
Revised 23 July 2017
Accepted 31 July 2017

Keywords:
Electromechanical
Pendulum
Magnet
Chaos

ABSTRACT

The paper is devoted to theoretical and experimental investigations of an electromechanical system consisting of DC motor, a physical pendulum with the repulsive magnets. The work consists of modeling, simulation and experimental measurements to validate the analytical predictions and the numerical simulation of the earlier introduced mathematical model. The parameters of the model are estimated using the experimental data. The analyzed system shows several types of non-linear effects, including hysteresis, jump phenomena, chaos and periodic dynamics. Good agreement between real and simulated behavior of the system is obtained.

© 2017 Elsevier Ltd. All rights reserved.

1. Introduction

Electromechanical systems play an essential role in fulfilling the needs of modern technological applications. The electrical energy supplied to these systems is transformed into mechanical energy with an efficiency of 80 per cent by electric drives [1]. Physicists are particularly interested in those kinds of the dynamical systems, since they are relatively simple but can exhibit almost all aspects and phenomena of non-linear dynamics. As consequence, the range of technological tasks that need these systems broadens every year.

This results in an increasing necessity for more advanced modeling, identification and control strategies for these systems. Many applications need a sufficiently concise and accurate description of the dynamics of these systems. This is especially true in automatic control applications. Dynamic models describing the electromechanical system in use can be developed using principles of physics. However, models constructed in this way may be difficult to derive due to lack of sufficient knowledge or uncertainties in system dynamics.

Given their numerous applications in engineering, many studies on the nonlinear dynamics of mechanical systems have been made. These mechanical systems are composed of pendulums in different configurations including planetary or spatial pendulums, simple or multiple, and sometimes parametrically excited pendulums [2–5]. In some case an experiment is performed in order to confirm analytical or numerical investigations [6–8]. Sometime, in order to achieve a good agreement between the model predictions and experimental data, one must take into account many details concerning physical modeling of the real process [9,10].

Mechanical structures such as models of pendulum-like lever arms and mechanical manipulators are increasingly attracting a lot of attention as their dynamical behavior has shown to exhibit different phenomena related to oscillations, bifurcation, and chaos. In the work [12], the authors investigated both numerically and experimentally an electromechanical system driven by a DC motor. The angular velocity of the mechanical part was almost constant because the power of the motor was relatively high. Mathematical modeling of the same system under simplifying conditions was presented in [13].

Electromechanical pendulums have important applications in space exploration, manufacturing automation, construction, mining, hazardous operations, and many other areas. Although significant progresses have been made in many aspects over the last one and half decade, many issues are not resolved yet, and further efforts and results in this area would contribute significantly to robotics, and in particular, automation. Research activities have

* Corresponding author:
E-mail address: na1bo@yahoo.fr (B. Nana).
URL: http://www.lamsebp.org (B. Nana)

http://dx.doi.org/10.1016/j.chaos.2017.07.027
0960-0779/© 2017 Elsevier Ltd. All rights reserved.

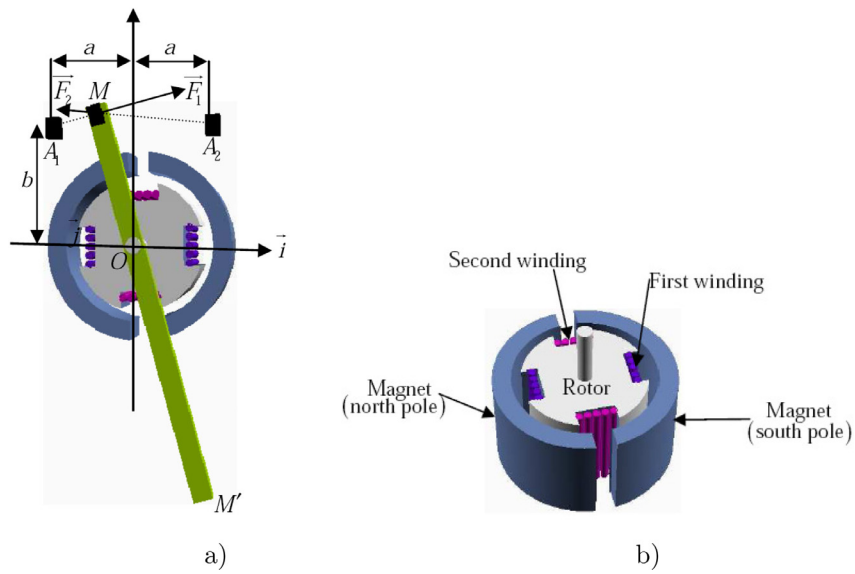

Fig. 1. a) Schematic representation of the pendulum system and b) schematic representation of the motor with windings to measure the angular velocity and the rotational angular of the rotor.

accordingly concentrated on the development of methodologies to cope with this [14–18]. The main purpose of this contribution is to present some results on the investigation about a nonlinear electromechanical system including a pendulum system electromagnetically actuated.

The main purpose of this contribution consists of the modeling, the simulation, the realization and experimental study of nonlinear electromechanical system including an electromagnetically actuated lever system. In the theoretical investigation, we use simple Newtonian physics to derive the equations of motion that describes the dynamics of the system. From these equations, time series and phase space plots are constructed and discussed. Both periodic and chaotic behaviors are observed, depending on the frequency and amplitude of the driver and the distance between the two magnets. The analytical prediction of chaos occurrence (not reported here) can be combined with the numerical simulations to give a proper insight to the studied dynamical system [11]. Amplitude jumps, hysteresis and bistable states occur for a range of frequencies near the natural frequency of the physical system. To solve the problem of low amplitudes of vibrations encountered by the author of reference [12], a DC motor of relatively low power is used in this work.

The paper is organized as follows. In Section 2, the physical description and the mathematical model of the system are given. In Section 3, the amplitude response is investigated and we present the results of our analytical calculations and numerical simulations. The effect of some parameters on the behavior of the system is analyzed in Section 4. In Section 5, the comparison between our simulations and experimental results are presented. Our conclusions are presented in the final section.

2. Physical description and mathematical modeling

2.1. Physical description

The system to be considered here is depicted in Fig. 1a). It is divided into three main parts: i) electrical motor - understood as object converting electrical energy to the mechanical one; ii) one-degree of freedom mechanical system; iii) three button magnets located at points A_1, A_2 and M. The only damping force that the model contains is inside the motor and it is characterized by a simple viscous damping function. Air resistance is neglected due to low velocities of vibrations and relatively large moments of inertia. Influence of the gravitational force is also included. The input signal being under control is voltage $u(t)$, while the coordinate $\theta(t) = (\widehat{\vec{j}\ \overrightarrow{OM}})$ describing the position of the mechanical system is considered as output.

The electrical motor is of the type permanent magnet and the diagram is shown in Fig. 1b). The permanent magnet motor uses a magnet to supply field flux. Permanent magnet DC motors have excellent starting torque capability with good speed regulation. The main advantages of using DC motors in such applications are ease of control for speed and position, wide range of operation, and ability to follow a set speed or position under load. Having these capabilities, these systems have been extensively used in many industrial applications [19]. However, when a DC motor rotates at relatively low speeds and in both directions, or when it works in a wide range of operation where high precision control is needed, the nonlinear effects on system behavior become far from negligible and may lead to intolerable modeling errors and poor control performance [20].

A disadvantage of permanent magnet DC motors is that they are limited to the amount of load they can drive. These motors can be found on low horsepower applications. As shown in the diagram, the rotor has two windings: the winding with blue cable carries electrical current to produce a mechanical torque while the winding with red cable is used to measure the back electromotive force which is related to the velocity of the mechanical system.

2.2. Mechanical system modeling

Unlike experimental setup, the mathematical model does not take into account impacts between magnets. That is why the full comparison of the theoretical model and experimental measurements can be performed for low amplitudes only, less than $\tan^{-1}\left(\frac{a}{b}\right)$.

A theoretical model is developed considering the six forces acting on the pendulum: the repulsive magnetic forces F_1 and F_2, the sinusoidal driving force applied by the motor, the damping force, the weight of the magnet located at point M and the weight of the pendulum. Let θ the angle between the meter stick and the horizontal axis.

The damping force is assumed to be proportional to the angular velocity of the pendulum, $\frac{d\theta}{dt}$. Then if β_m is the damping coefficient, the damping torque can be defined as follows:

$$\Gamma_d = -\beta_m \frac{d\theta}{dt}. \tag{1}$$

The magnets are considered to be point magnets. As for the two magnets located at A_1 and M, the two magnets located at A_2 and M are oriented with like poles facing each other. For simplicity of our theoretical model, we assume that the magnetic force is a repulsive force between two point magnets with an inverse squared dependence on distance, and it is thus a function of the angular displacement of the pendulum θ. Let $OM = \ell_1$ and $OM' = 2\ell - \ell_1$, then the magnetic forces $\vec{F_1}$ and $\vec{F_2}$ produced respectively by the magnets A_1 and A_2 on M are given as:

$$\begin{aligned}\vec{F_1} &= \frac{\mu_0 q_1 q_2}{4\pi} \frac{\overrightarrow{A_1M}}{A_1M^3} \\ &= \frac{\mu_0 q_1 q_2}{4\pi} \frac{(a - \ell_1 \sin\theta)\,\vec{i} - (b - \ell_1 \cos\theta)\,\vec{j}}{\left[a^2 + b^2 + \ell_1^2 - 2\ell_1 a \sin\theta - 2b\ell_1 \cos\theta\right]^{\frac{3}{2}}},\end{aligned} \tag{2}$$

$$\begin{aligned}\vec{F_2} &= \frac{\mu_0 q_1 q_2}{4\pi} \frac{\overrightarrow{A_2M}}{A_2M^3} \\ &= \frac{\mu_0 q_1 q_2}{4\pi} \frac{(-a - \ell_1 \sin\theta)\,\vec{i} - (b - \ell_1 \cos\theta)\,\vec{j}}{\left[a^2 + b^2 + \ell_1^2 + 2\ell_1 a \sin\theta - 2b\ell_1 \cos\theta\right]^{\frac{3}{2}}}.\end{aligned} \tag{3}$$

Here, μ_0 is the permeability of vacuum, q_1 is the pole strength of magnet M and q_2 is the pole strength of magnets A_1 and A_2. With $\delta_1 = \frac{a}{\ell_1}$ and $\delta_2 = \frac{b}{\ell_1}$, the magnetic torques Γ_1 and Γ_2 produced by the magnetic forces $\vec{F_1}$ and $\vec{F_2}$ have respectively the following expressions:

$$\Gamma_1 = \frac{\mu_0 q_1 q_2}{4\pi \ell_1} \frac{\delta_2 \sin\theta - \delta_1 \cos\theta}{\left(1 + \delta_1^2 + \delta_2^2 - 2\delta_1 \sin\theta - 2\delta_2 \cos\theta\right)^{\frac{3}{2}}}, \tag{4}$$

$$\Gamma_2 = \frac{\mu_0 q_1 q_2}{4\pi \ell_1} \frac{\delta_2 \sin\theta + \delta_1 \cos\theta}{\left(1 + \delta_1^2 + \delta_2^2 + 2\delta_1 \sin\theta - 2\delta_2 \cos\theta\right)^{\frac{3}{2}}}. \tag{5}$$

Let m_0 and m the masses of the magnet located at M and the meter stick respectively, the torques Γ_3 and Γ_4 produced by their corresponding weights are given respectively as:

$$\Gamma_3 = \ell_1 m_0\, g \sin\theta, \tag{6}$$

$$\Gamma_4 = -(\ell - \ell_1) m g \sin\theta. \tag{7}$$

where g is the acceleration due to gravity. The last torque is that produced by the electric motor. It is expressed as follows:

$$\Gamma = hDB_m Ni, \tag{8}$$

where h and D are respectively the height and diameter of the rotor, B_m is the magnetic flux density produced by the magnets inside the motor, N is the number of turns and i is the current through the coil.

Newton's second law is applied to the rotating rigid body and thus the equation of motion takes the form given below

$$J_m \frac{d^2\theta}{dt^2} = \Gamma_d + \Gamma_1 + \Gamma_2 + \Gamma_3 + \Gamma_4 + \Gamma, \tag{9}$$

where $J_m = m\left(\frac{4}{3}\ell^2 - 2\ell\ell_1 + \ell_1^2\right) + m_0\ell_1^2$ is the moment of inertia of the pendulum arm with the fixed magnet. By combining Eqs. (1), (4), (5), (6), (7), (8) and (9) we arrive at the equations of motion in the form of a system of coupled differential equations

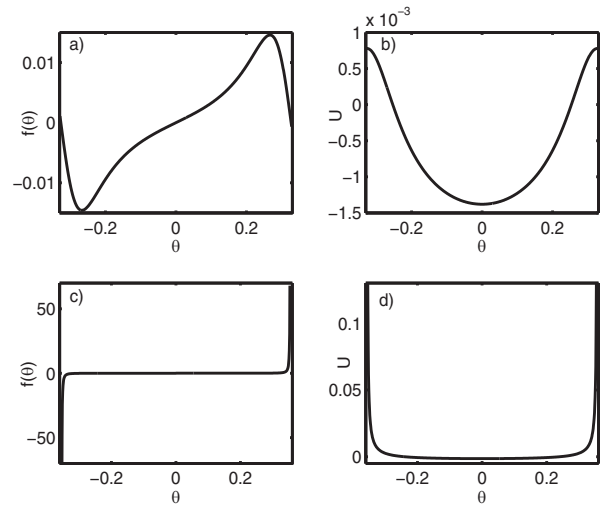

Fig. 2. Behavior of f and the corresponding potential U for $-\theta_{\max} \leqslant \theta \leqslant \theta_{\max}$. a) f versus θ for $\delta_1^2 + \delta_2^2 \neq 1$, b) potential U versus *theta* for $\delta_1^2 + \delta_2^2 \neq 1$, c) f versus θ when $\delta_1^2 + \delta_2^2 = 1$, d) potential U versus *theta* when $\delta_1^2 + \delta_2^2 = 1$.

$$\begin{aligned}J_m \frac{d^2\theta}{dt^2} &+ \beta_m \frac{d\theta}{dt} + \frac{\mu_0 q_1 q_2}{4\pi\ell} f_1(\theta) \\ &+ (mg\ell - mg\ell_1 - m_0 g\ell_1)\sin\theta = hDB_m Ni,\end{aligned} \tag{10}$$

with the function $f_1(\theta)$ defined as

$$\begin{aligned}f_1(\theta) = &\frac{\delta_1 \cos\theta - \delta_2 \sin\theta}{\left(1 + \delta_1^2 + \delta_2^2 - 2\delta_1 \sin\theta - 2\delta_2 \cos\theta\right)^{\frac{3}{2}}} \\ &- \frac{\delta_1 \cos\theta + \delta_2 \sin\theta}{\left(1 + \delta_1^2 + \delta_2^2 + 2\delta_1 \sin\theta - 2\delta_2 \cos\theta\right)^{\frac{3}{2}}}.\end{aligned} \tag{11}$$

2.3. Modeling the electric motor

The voltage/current relationship for the armature windings of the motor is

$$L\frac{di}{dt} + Ri + e(t) = u(t), \tag{12}$$

where $u(t)$ is the input voltage, i is the current through the winding, R is the armature resistance, L is the inductance of the winding, $e(t)$ is the back electromotive force. They are expressed as

$$\begin{aligned}u(t) = E_m \sin(\omega t),\ L = \frac{\mu_0 \mu_r N^2 hD}{\ell_g},\ R = \frac{8\varphi(h + D)N}{\pi d^2},\ e(t) \\ = hDB_m N \frac{d\theta}{dt}\cos\theta.\end{aligned} \tag{13}$$

E_m and ω are respectively the magnitude and the radian frequency of the applied voltage source, μ_r is the relative permeability of the rotor, ℓ_g is the thickness of the winding, φ and d are respectively the resistivity and diameter of the wire used in the winding.

2.4. Completed mathematical model

To conveniently describe the system, the dimensionless equations of the electric motor and the mechanical part are established using the transformations $t = \omega_0\tau$ and $i = I_0 x$, where τ and x are dimensionless variables. The mathematical model of the nonlinear electromechanical device can then be written as follows:

$$\ddot{\theta} + \lambda_m \dot{\theta} + f(\theta) = \varepsilon_m x, \tag{14}$$

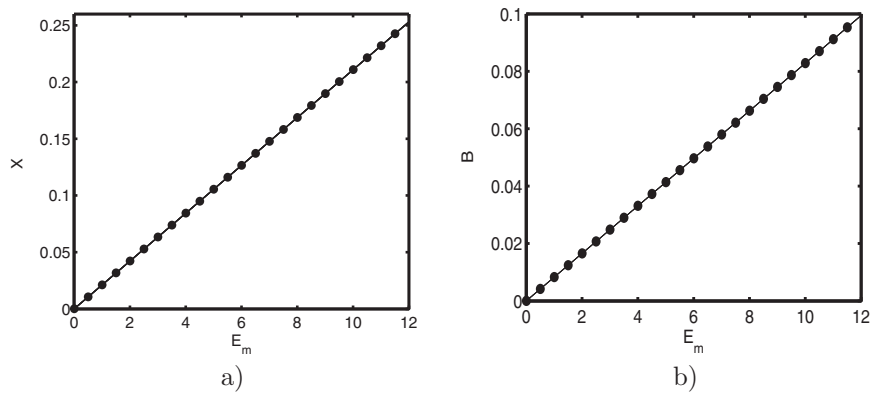

Fig. 3. a) Amplitude of current X versus the amplitude of the generator E_m. b) amplitude of angle B versus the amplitude of the generator E_m. The curves with full line are our analytical results while the curves with dots are obtained numerically.

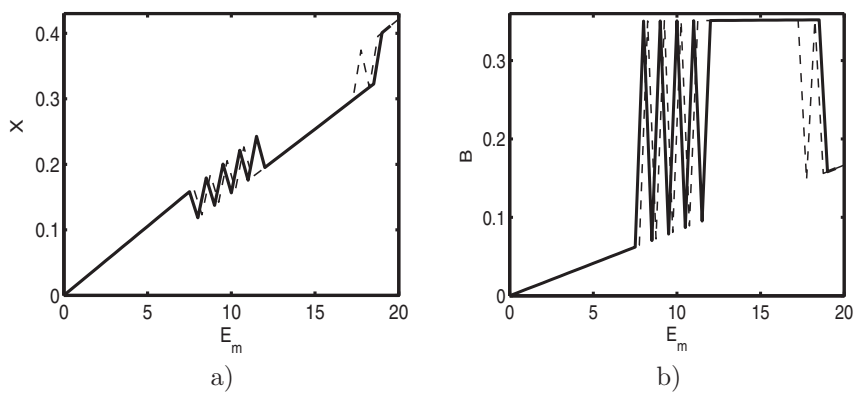

Fig. 4. a) Amplitude of current X versus the amplitude E_m of the generator. b) amplitude of angle B versus the amplitude E_m of the generator. The curves with full line are obtained when increasing the amplitude and the curves with dashed line are obtained when decreasing the frequency.

$$\dot{x} + \lambda_e x + \varepsilon_e \dot{\theta} \cos\theta = E \sin(\Omega\tau), \tag{15}$$

with the function $f(\theta)$ and the following new introduced parameters defined respectively as:

$$f(\theta) = \gamma_1 f_1(\theta) + \gamma_2 \sin(\theta), \tag{16}$$

$$\lambda_e = \frac{R}{L\omega_0},\ E = \frac{E_m}{L\omega_0 I_0},\ \Omega = \frac{\omega}{\omega_0},\ \varepsilon_e = \frac{hDB_m N}{LI_0},\ \lambda_m = \frac{\beta_m}{J_m\omega_0},\ \gamma_1 = \frac{\mu_0 q_1 q_2}{4\pi J_m \omega_0^2 \ell_1}, \varepsilon_m = \frac{hDB_m N}{J_m\omega_0^2} I_0, \gamma_2 = \frac{g}{J_m\omega_0^2}(m\ell - m\ell_1 - m_0\ell_1). \tag{17}$$

3. Theoretical investigation

3.1. Dynamics of the model

To prevent impacts between magnets, we have to choose the parameters of the system such a way that when the pendulum reaches it maximum fixed angle $\theta_{\max} = \tan^{-1}(\frac{a}{b}) = \tan^{-1}(\frac{\delta_1}{\delta_2})$, the repulsive magnetic force becomes infinite. For that purpose, the denominators of $f(\theta = \theta_{\max})$ must be zero. After some mathematical manipulations, we obtain the following condition:

$$-\theta_{\max} \leqslant \theta \leqslant \theta_{\max} \Rightarrow \delta_1^2 + \delta_2^2 = 1. \tag{18}$$

To verify the condition given in Eq. (18), the graphs of the function $f(\theta)$ and the corresponding potential are plotted in Fig. 2. The curves of Fig. 2a) and 2b) reveal that when $\delta_1^2 + \delta_2^2 \neq 1$ ($\delta_1 = 0.348$, $\delta_2 = 1.03$), the repulsive force can be zero when the angle reaches the maximum value and then according to the form of the potential, the point M can move out of the interval $-\theta_{\max} \leqslant \theta \leqslant \theta_{\max}$. In contrast, Figs. 2c) and 2d) show that for $\delta_1^2 + \delta_2^2 = 1$ ($\delta_1 = 0.348$, $\delta_2 = 0.937$), the repulsive force and the corresponding potential grow to infinity when the rotational angle comes close to the maximum value. For this reason, M is constrained to move in the required region.

To study the dynamics of the model, the solutions of the equations of motion of the nonlinear electromechanical device need to be found. For analytical investigation, we use Eq. (18) and we expand $f(\theta)$ with the result

$$f(\theta) = c_0\theta + c_1\theta^3 \text{ with } c_0 = \gamma_1 \frac{\delta_2 + 3}{(2 - 2\delta_2)^{\frac{3}{2}}} + \gamma_2 \text{ and } c_1 = \gamma_1 \frac{\delta_2^2 + 38\delta_2 + 57}{12(2 - 2\delta_2)^{\frac{5}{2}}} - \frac{\gamma_2}{6}. \tag{19}$$

Eqs. (14) and (15) are not readily amenable to a closed-form solution. We, therefore, resort to perturbation methods to obtain an approximate analytical solution. In the harmonic state, the time evolution of current and angle can be described as

$$x = X_1 \cos(\Omega\tau) + X_2 \sin(\Omega\tau), \tag{20}$$

$$\theta = B_1 \cos(\Omega\tau) + B_2 \sin(\Omega\tau). \tag{21}$$

Let us set $X = \sqrt{X_1^2 + X_2^2}$ and $B = \sqrt{B_1^2 + B_2^2}$ the amplitude of current and the amplitude of the mechanical displacement respectively. Using the harmonic balance method, we insert Eqs. (20) and (21) into Eqs. (14) and (16), and after some algebraic manipulations, it comes that the amplitudes X and B satisfy the following

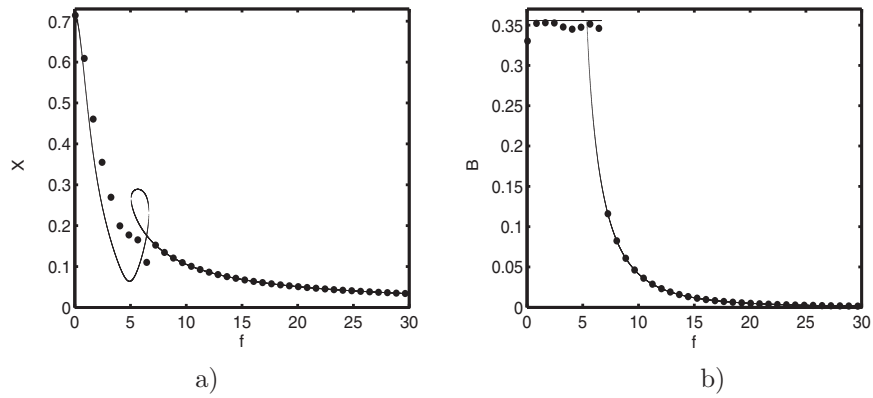

Fig. 5. a) Amplitude of current X versus the frequency f of the generator. b) amplitude of angle B versus the frequency f of the generator. The curves with full line are our analytical results while the curves with dots are obtained numerically.

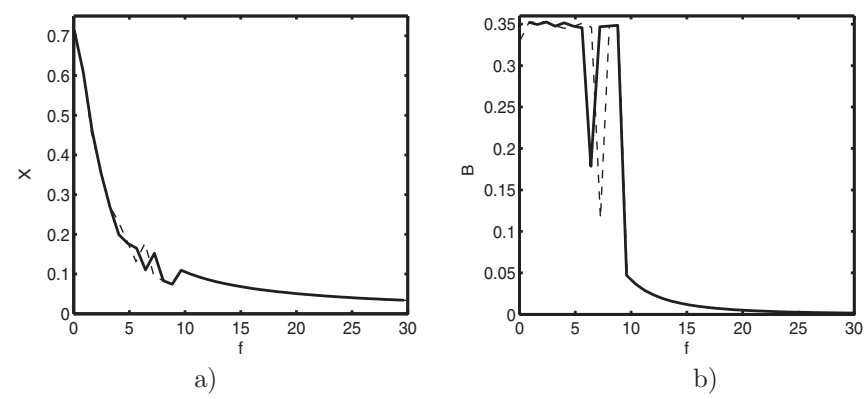

Fig. 6. a) Amplitude of current X versus the frequency f of the generator. b) amplitude of angle B versus the frequency f of the generator. The curves with full line are obtained when increasing the frequency and the curves dashed line are obtained when decreasing the frequency.

equations:

$$X = \frac{B}{\varepsilon_m}\sqrt{\left(\Omega^2 - c_0 - \frac{3}{4}c_1B^2\right)^2 + \lambda_m^2\Omega^2} \quad \text{and} \quad B = \sqrt{\mathfrak{B}}, \tag{22}$$

$$a_3\mathfrak{B}^3 + a_2\mathfrak{B}^2 + a_1\mathfrak{B} + a_0 = 0. \tag{23}$$

The new coefficients a_3, a_2, a_1 and a_0 are defined as follow:

$$\begin{aligned} a_3 &= 9c_1^2\left(\Omega^2 + \lambda_e^2\right), \\ a_2 &= -24c_1\left[\Omega^4 + \Omega^2\left(\lambda_e^2 - c_0 - \varepsilon_e\varepsilon_m\right) - c_0\lambda_e^2\right], \\ a_1 &= 16\left[\Omega^2\left(\Omega^2 - \varepsilon_e\varepsilon_m - c_0\right)^2 + \lambda_m^2\Omega^2\left(\Omega^2 + \lambda_e^2\right)\right] \\ &\quad +16\left[\lambda_e^2\Omega^4 + 2\Omega^2\varepsilon_e\varepsilon_m(\lambda_e\lambda_m + c_0) + (\lambda_e c_0)^2\right], \\ a_0 &= -(4\varepsilon_m E)^2. \end{aligned} \tag{24}$$

To derive solutions of Eq. (23), let us consider the following parameters σ and ν, and determinant Δ:

$$\sigma = a_2^2 - 3a_3a_1, \quad \nu = \frac{2a_2^3 - 9a_3a_2a_1 + 27a_3^2a_0}{2}, \quad \Delta = \nu^2 - \sigma^3.$$

As odd degree polynomial, Eq. (23) can have one or three real solutions according to the sign of Δ.

If $\Delta \geq 0$, Eq. (23) has one real solution

$$B = \sqrt{\frac{-a_2 + \sqrt[3]{\nu - \sqrt{\Delta}} + \sqrt[3]{\nu + \sqrt{\Delta}}}{3a_3}}. \tag{25}$$

If $\Delta < 0$, Eq. (23) has three real solutions given as follows:

$$B_1 = \sqrt{\frac{-a_2 + 2\sqrt{\sigma}\cos\left(\frac{\alpha - 2\pi}{3}\right)}{3a_3}}, \quad B_2 = \sqrt{\frac{-a_2 + 2\sqrt{\sigma}\cos\left(\frac{\alpha}{3}\right)}{3a_3}},$$
$$B_3 = \sqrt{\frac{-a_2 + 2\sqrt{\sigma}\cos\left(\frac{\alpha + 2\pi}{3}\right)}{3a_3}} \quad \text{where} \quad \alpha = \arctan\left(\frac{\sqrt{-\Delta}}{\nu}\right). \tag{26}$$

Even if the analytical method gives rise to several solutions, it remains that for the stability of the electric motor the appropriate solution will be the one with smallest amplitude of current.

3.2. Parameters estimation

Some parameters are relatively easy to obtain by the use of direct mass and lengths measurements or simple calculations, and they are assumed constant throughout the estimation process. The major difficulty in obtaining convergence between experiment and simulation has been in finding the "right" set of parameters β_m and μ_r. Many different sets were tried before good agreement was obtained. The experimental parameters are given in Table 1.

3.3. Effect of some parameters

In order to confirm the approximation done in (19), (20) and (21), a comparison of numerical simulations with analytical investigations for the stationary response is done. If the amplitude E_m and frequency $f = \omega/2\pi$ of the excitation are given, the amplitudes X and B of the responses can be approximately obtained

Table 1
Values of the experimental parameters.

Parameters	Values	Parameters	Values
ℓ	$13.35 \cdot 10^{-2}$ m	ℓ_1	$5.80 \cdot 10^{-2}$ m
a	$2.02 \cdot 10^{-2}$ m	b	$5.44 \cdot 10^{-2}$ m
h	$9.85 \cdot 10^{-2}$ m	d	$0.15 \cdot 10^{-3}$ m
D	$8.12 \cdot 10^{-2}$ m	ℓ_g	$5.0 \cdot 10^{-3}$ m
m	$5.0 \cdot 10^{-3}$ Kg	β_m	$2.12 \cdot 10^{-4}$ Ns
q_1	5.19 Am	$m_{01} = m_0$	$5.50 \cdot 10^{-3}$ Kg
q_2	6.02 Am	m_{02}	$5.58 \cdot 10^{-3}$ Kg
φ	$1.72 \cdot 10^{-8}$ Ωm	μ_r	985
N	20	B_m	0.73 T
R_1	$10K\Omega$	C_1	100μF
g	9.82 N/Kg	-	-

using Eqs. (22), (25) or (26). For our first verification, we have maintained constant the frequency of the external generator $f = 10$ Hz. We have analyzed the behavior of the system when varying the amplitude of the external generator from 0 V up to 12 V. Fig. 3 shows the variation of X and B versus the amplitude E_m both from the above analytical expression (full line) and from the direct numerical simulation of the differential Eqs. (14) and (16) using the fourth order Runge-Kutta method (curves with points).

For moderated and high values of frequency, the amplitude of current and the amplitude of the mechanical displacement increase linearly with the amplitude of the generator. As the graphs reveal, good agreements are found between the analytical and simulation results.

But for low values of frequency, the jump phenomenon are found in the simulations results as shown in the graphs of Figs. 4a) and 4b) for high values of the applied voltage source.

To obtain these curves, the final system states of the previously iterated value of the amplitude E_m is chosen as the initial condition for the next system iteration with the new value of the amplitude. The important phenomenon which occurs with this nonlinear system is the so-called hysteresis or jump phenomenon which occurs because of the multi-valued properties of the response due to the nonlinearity. For the system under study, hysteresis can occur by either changing the amplitude or the frequency of the external excitation. With $f = 10.0$ Hz, Fig. 4 shows the behavior of X and B for a range 0 V $\leq E_m \leq$ 20 V sweeping both up and down.

In Fig. 5, we show the amplitude of current through the electric motor and the amplitude of the mechanical displacement for $E_m =$ 5.0 V for a range of frequencies 0 Hz $\leq f \leq$ 30 Hz. As in the curves of Fig. 3, the analytical solutions are plotted with full line while the simulation results are plotted with points.

As shown on the graph, the amplitude of current and the amplitude of the mechanical displacement decrease when the frequency increases. Also notice the multiple amplitudes of current as well as of mechanical displacement when the frequency is between 5.08 Hz and 6.65 Hz. This will be shown as two unstable solutions separated by a stable solution. Even here, a good agreement is found between our analytical and simulation results.

As mentioned above, the hysteresis can be obtained by changing the frequency of the external excitation as shown in Fig. 6.

The curves with full line are obtained when increasing the frequency and the curves with dashed line are obtained when decreasing the frequency. As shown, the hysteresis phenomenon appears on the two curves. According to Fig. 6a) and 6b), as we increase the frequency, the amplitude of current and the amplitude of the mechanical displacement follow a certain path different to that obtained when we decrease the frequency.

To obtain these curves, the final system states of the previously iterated value of the frequency f is chosen as the initial condition for the next system iteration with the new value of the frequency.

At this stage, it is interesting to analyze the effect of the magnetic pole strength q_2 on the dynamics of the system. For that purpose, we kept constant the amplitude and the frequency of the external generator as $E_m = 5$ V and $f = 10$ Hz. Then, Fig. 7 shows the amplitude of current and the amplitude of the angle when q_2 is increased from 0 up to 1000 Am.

We notice from Fig. 7a) that the amplitude of current increases slightly with the magnetic pole strength q_2. While the amplitude of the mechanical displacement starts to increase when q_2 increases and decreases after a certain value of q_2. The jump and the resonance phenomena observed in the current response and angle response respectively can be understood. In fact, the resonant frequency of the mechanical part is proportional through the parameter γ_1 to the magnetic pole strength q_2 as shown by Eqs. (14) and (22).

We can notice in this section that the results show good agreement between the analytical treatment and the numerical simulations.

3.4. Dynamics of the model

The plethora of different dynamical behaviors exhibited by the system can be best summarized by looking at the system's bifurcation diagrams. Fig. 8 shows a two-parameter bifurcation diagram illustrating the dependence of the dynamical behavior of the system on the two control parameters E_m and f.

The bifurcation diagram has been obtained by extensive simulation of the system throughout the parameter space (E_m, f). The resulting trajectories are analyzed in order to establish whether the system, at steady-state, settles to an equilibrium point, a limit cycle or a chaotic attractor. In practice, for each parameter combination, the system is simulated by numerical integration for a sufficiently long time and the transient is discarded.

In Fig. 8, different behaviors are denoted by different "colors". The brown area denotes the period-1 limit cycle which includes the near-sinusoidal oscillation mode. The red area, the green area, the yellow area and the blue areas denote respectively the period-2, period-3, period-4 and period-5 behaviors of the system. While the magenta area indicates a combination of period-6, period-7 and period-8. The chaotic dynamics is indicated by the cyan area where no periodic behavior was detected. Finally, the white area is used for the unbounded oscillation as the point M moves out of the region $-\theta_{\max} \leq \theta \leq \theta_{\max}$ defined above.

We note in Fig. 8 the presence of a large region of complex behavior in the parameter space where the system undergoes several bifurcations when varying either of the parameters E_m and f.

The characteristic dynamical behaviors are secondly investigated by varying the parameter q_2. The bifurcation diagram as well as the Lyapunov exponent respectively drawn in Fig. 9a) and Fig. 9b) show that for certain sets of parameters, the system exhibits chaotic oscillations. We used as control parameter q_2 and the frequency as well as the amplitude is maintained constant as $f = 5$ Hz and $E_m = 10$ V.

The system response comes into a chaotic motion when q_2 lies between 2.91 Am and 16.15 Am, returns to the periodic motion when 16.15 Am $\leq q_2 \leq$ 16.86 Am, 17.56 Am $\leq q_2 \leq$ 24.17 Am and 34.59 Am $\leq q_2 \leq$ 40 Am. Chaos is confirmed by the variation of the Lyapunov exponent in Fig. 9b). As shown, there is a good agreement between the bifurcation diagram and its corresponding maximal Lyapunov exponent. To present the route to chaos from a periodic motion, the variation in the state variable θ with respect to the control parameter q_2 is plotted in Fig. 10.

The period doubling route to chaos with different jumping phenomena are observed in the system, through decreasing the control parameter q_2 from 50 Am to 33 Am while holding the frequency and the magnitude of the external excitation constant.

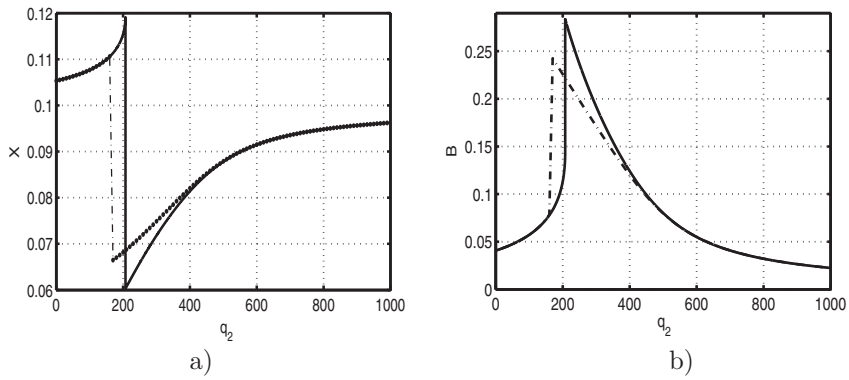

Fig. 7. a) Amplitude of current X versus the magnetic pole strength q_2. b) Amplitude of angle B versus the magnetic pole strength q_2. The curves with full line are our analytical results while the curves with dashed line are obtained numerically.

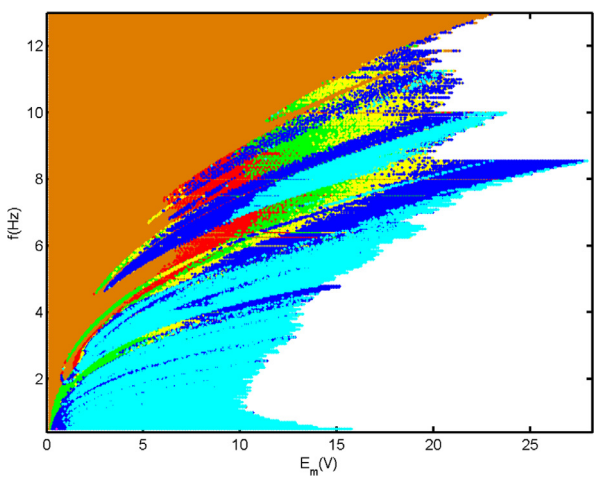

Fig. 8. Two-parameter bifurcation diagram showing the dynamical behavior of the system in the plane (E_m, f).

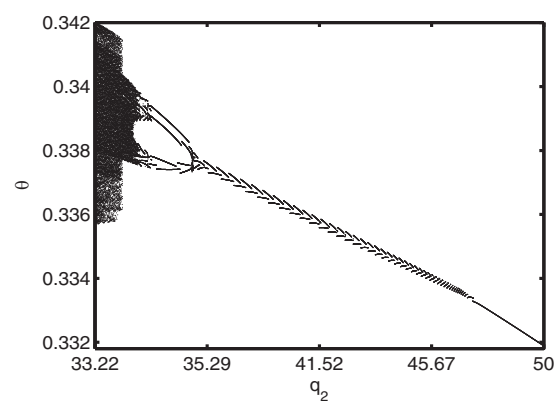

Fig. 10. Zoom on the bifurcation diagram at function of q_2 for $E_m = 10$ V and $f = 5$ Hz.

4. Experiment

4.1. Experimental setup

Fig. 11a) presents the complete experimental setup of the system studied theoretically and described in the previous part of the paper while a zoom on the electrical part is shown in Fig. 11b).

A voltage generator **(7)** supplies one winding of the DC motor **(1)**. As mentioned above, the second winding is used to measure the angular displacement θ. In fact, the induced electromotive force $e_2(t)$ recorded at the second winding terminals is given as follows:

$$e_2(t) = hDB_mN\frac{d\theta}{dt}\cos\theta \tag{27}$$

From Eq. (27), we can deduce that the induced electromotive force is proportional to the angular velocity $\dot{\theta}$ for small values of the

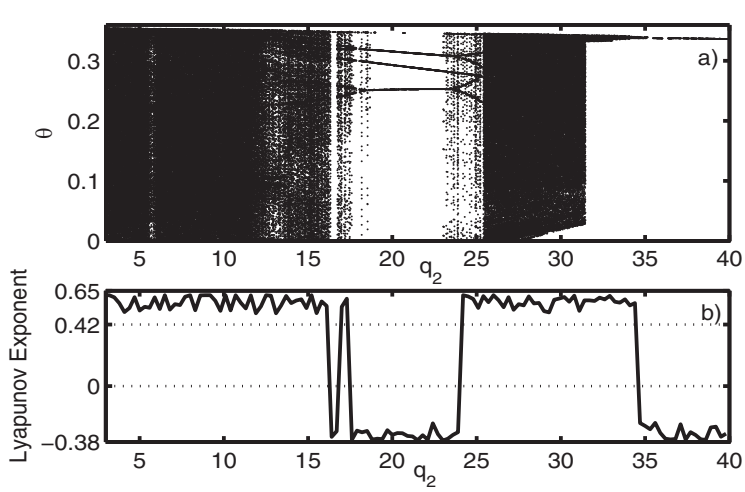

Fig. 9. a) Bifurcation diagram and b) Lyapunov exponent, both at function of q_2 for $E_m = 10$ V and $f = 5$ Hz.

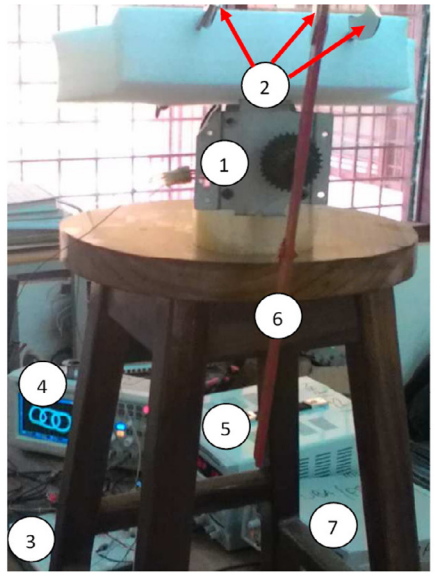

a)

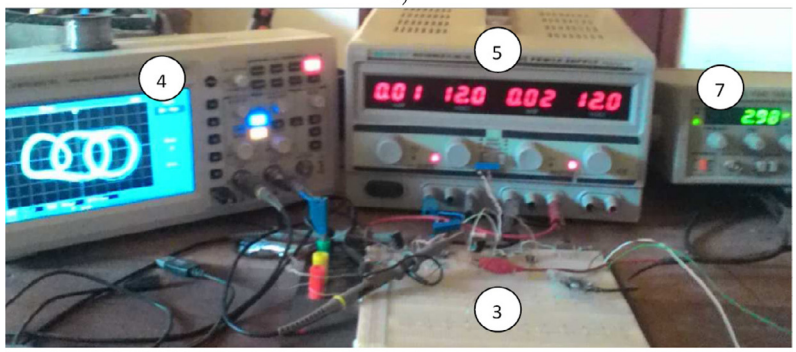

b)

Fig. 11. a) Complete experimental setup, b) Zoom on the electrical part.

angular displacement θ. Then, by using an integrator circuit **(3)** formed by the operational amplifiers (TL082), a resistor R_1 and a capacitor C_1, we obtain an output voltage v_s that is proportional to the angular displacement. We have

$$v_s(t) = -\frac{1}{R_1C_1}\int e_2(t)dt = -\frac{hDB_mN}{R_1C_1}\sin\theta \simeq -\frac{hDB_mN}{R_1C_1}\theta \qquad (28)$$

The power supply **(5)** is used as polarization voltage of the operational amplifiers. It was not possible to visualize the output signals using the analog oscilloscope because of the very low operating frequencies of the system. The digital oscilloscope **(4)** allows immediate viewing of the time series and phase space plots of the pendulum motion. The three magnets **(2)** and the pendulum **(6)** are also indicated. The values of al the parameters are given in Table 1.

4.2. Experimental and numerical results

From the two bifurcation diagrams shown previously, it can be seen that for different values of the frequency f and amplitude E_m of the external generator, periodic motion and chaotic motion appear alternately. Phase portraits are shown under different f and E_m and the experimental results are compared to the simulation ones.

The experimental investigations of the systems showed that it can also exhibit regular and irregular behaviors. For example, when the amplitude of the external excitation is $E_m = 4.5$ V and the frequency is $f = 7$ Hz, the system leads to regular dynamics, with angular oscillations of amplitude $\theta_m = 0.117\text{rad} \simeq 6.71^o$ as presented in Fig. 12a).

As we reduce the frequency experimentally, a jump is observed when $f = 6.68$ Hz. To verify this behavior, we show in the graph of Fig. 13a) the phase portrait of pendulum system for $E_m = 4.5$ V and $f = 6.68$ Hz. As the graph reveals, the system leads to regular dynamics with a jump of amplitude at $\theta_m = 0.35\text{rad} \simeq 20.66^o$.

For comparison, the experimental result is shown in Fig. 13b).

According to their shapes, there is a small difference between the experimental and simulation results. We are thinking that the difference is due to the fact that the magnets are considered point magnets. However, according to the periodicity, they are confirmed quantitatively very well by the developed mathematical model and its numerical simulations.

Proceeding in the same manner, Figs. 14a), 15a), 16a) and 17a) are obtained from direct numerical simulations of Eqs. (14) and (16) respectively for the following values of the frequency: $f = 5.3$ Hz, $f = 4.5$ Hz, $f = 3.65$ Hz and $f = 2.47$ Hz. To verify these results, the corresponding experimental results are plotted in Figs. 14b), 15b), 16b) and 17b).

One can easily note the good agreement between numerical and experimental results as the regular and chaotic behaviors of the system are confirmed by the two results. The experimental setup has up to three control parameters that are experimentally

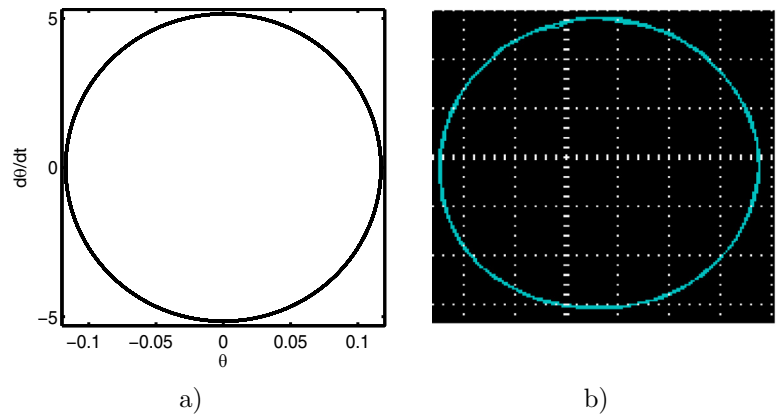

Fig. 12. Phase portrait of the pendulum system when $E_m = 4.5$ V and $f = 7.0$ Hz: a) numerical plot and b) experimentally obtained.

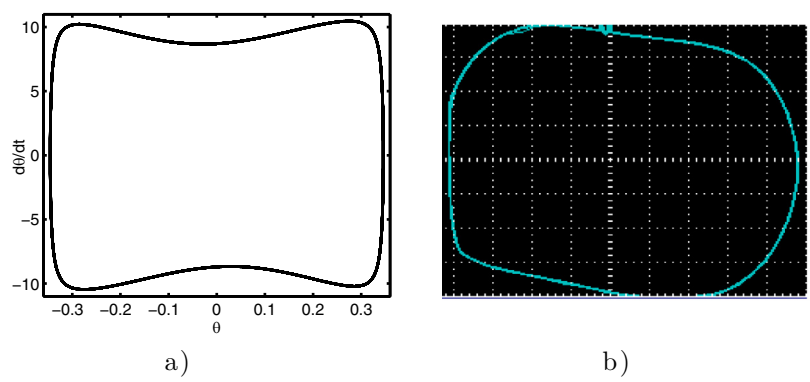

Fig. 13. Phase portrait of the pendulum system when $E_m = 4.5$ V and $f = 6.68$ Hz: a) numerical plot and b) experimentally obtained.

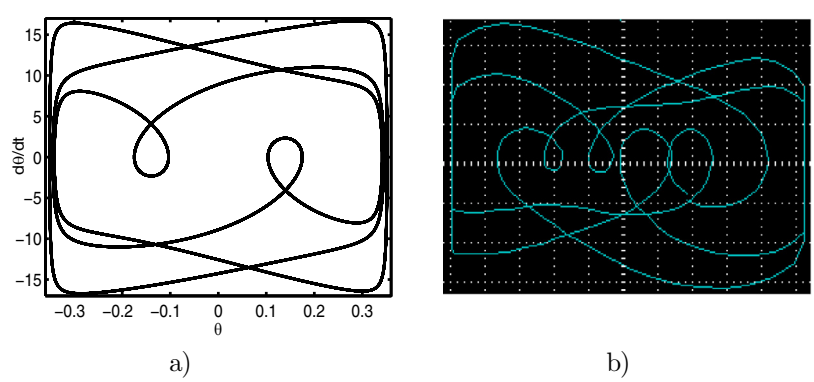

Fig. 14. Phase portrait of the pendulum system when $E_m = 4.5$ V and $f = 5.3$ Hz: a) numerical plot and b) experimentally obtained.

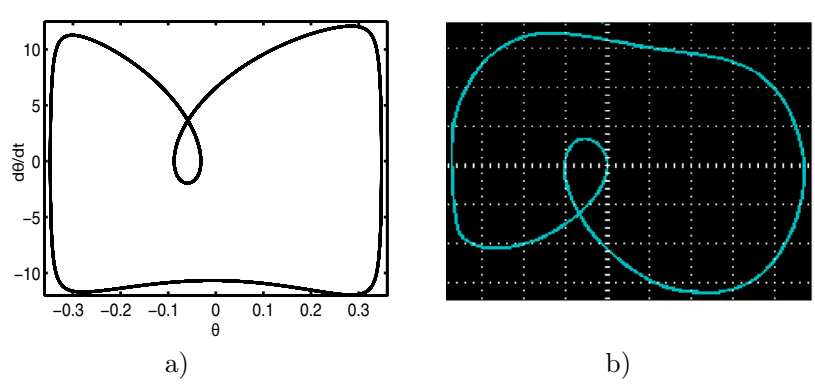

Fig. 15. Phase portrait of the pendulum system when $E_m = 4.5$ V and $f = 4.5$ Hz: a) numerical plot and b) experimentally obtained.

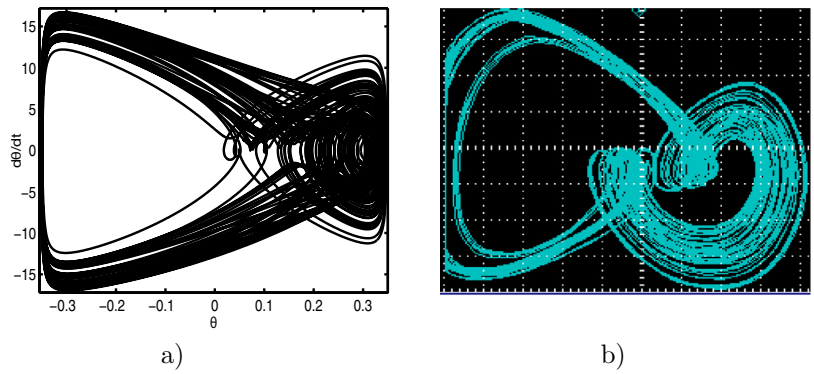

Fig. 16. Phase portrait of the pendulum system when $E_m = 4.5$ V and $f = 3.65$ Hz: a) numerical plot and b) experimentally obtained.

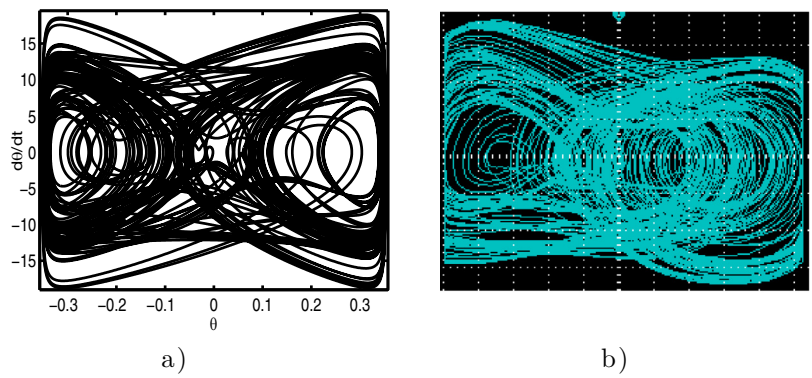

Fig. 17. Phase portrait of the pendulum system when $E_m = 4.5$ V and $f = 2.47$ Hz: a) numerical plot and b) experimentally obtained.

accessible in real time: the frequency f and the amplitude E_m of the generator and the relative position a of the magnets in a vertical plane.

5. Conclusion

This paper has dealt with the theoretical and experimental studies of pendulum system in a repulsive magnetic field. We have determined analytically the amplitude of current through the electric motor and the amplitude of the mechanical displacement. Periodic and chaotic behaviors are investigated for different values of the control parameters such as amplitude and frequency of the external excitation. Also presented here are the characteristic features of nonlinear systems such as bistable states, amplitude jumps, and hysteresis. Good agreements are found between theoretical and experimental results.

The system holds much promise for further studies since not all of the above control parameters are examined in this paper. The analytical prediction of chaos occurrence in such system under different voltage sources is another interesting task [11]. Furthermore, the experimental setup is simple and inexpensive to build, making it a suitable and affordable experiment.

References

[1] Kolesnikov AA. Modern applied control theory: new classes of technical systems regulators. TSURE press, Taganrog 2000;2.
[2] Przybylska M, Szuminski W. Non-integrability of flail triple pendulum, chaos. Solitons Fractals 2013;53:60–74.
[3] Chen Y, Wu X, Liu Z. Global chaos synchronization of electro-mechanical gyrostat systems via variable substitution control, chaos. Solitons Fractals 2009;42:1197–205.
[4] Polo MFP, Molina MP, Chica JG. Chaotic dynamic and control for micro-electro-mechanical systems of massive storage with harmonic base excitation, chaos. Solitons Fractals 2009;39:1356–70.
[5] Meng G, Zhang W, Huang H, Li HG, Chen D. Micro-rotor dynamics for micro–electro-mechanical systems (MEMS), chaos. Solitons Fractals 2009;40:538–62.
[6] Francisco HI, Ferreira AM, Savi MA. Chaos control in a nonlinear pendulum using a semi-continuous method, chaos. Solitons Fractals 2004;22:653–68.
[7] Awrejcewicz J, Supe B, Kudra G, Wasilewski G, Olejnik P. Numerical and experimental study of regular and chaotic motion of triple physical pendulum. Int J Bifurcation Chaos 2008;18:2883–915.
[8] Aline SP, Savi MA. Controlling chaos in a nonlinear pendulum using an extended time-delayed feedback control method, chaos. Solitons Fractals 2009;42:2981–8.
[9] Curiac DI, Volosencu C. A 2d chaotic path planning for mobile robots accomplishing boundary surveillance missions in adversarial conditions. Commu Nonlinear Sci Numer Simulat 2014;19:3617–27.
[10] Belato D, Weber HI, Balthazar JM, Mook DT. Chaotic vibrations of a nonideal electro-mechanical system. Int J Solids Struct 2001;38:1699–706.
[11] Awrejcewicz J, Sendkowski D. How to predick stick-slip chaos in r^4. Phys Lett A 2004;330:371–6.
[12] Avanço RH, Navarro HA, Brasil RM, Balthazar JM. Nonlinear dynamics of a pendulum excited by a crank-shaft-slider mechanism. Int Mech Eng Congr Exposition 2014;4.
[13] Cveticanin L. Dynamics of the non-ideal mechanical systems. J Serbian Soc Comput Mech 2010;4:75–86.
[14] Kazmierczak M, Kudra G, Awrejcewicz J, Wasilewski G. Numerical and experimental investigation of bifurcational dynamics of an electromechanical system consisting of a physical pendulum and DC motor. Dynamical Systems - Applications TU of Lodz Press, Lodz 2013;73:49–58.
[15] Kazmierczak M, Kudra M, Kazmierczak G, Awrejcewicz J, Wasilewski G. Mathematical modelling, numerical simulations and experimental verification of bifurcation dynamics of a pendulum driven by a dc motor. Eur J Phys 2015;36:1–13.
[16] Kitio KCA, Woafo P. Dynamics of a self-sustained electromechanical system with flexible arm and cubic coupling. Commun Nonlinear Sci Numer Simulat 2007;12:1504–17.
[17] Ning H, Qingjie C. Global bifurcations of a rotating pendulum with irrational nonlinearity. Commun Nonlinear Sci Numer Simulat 2016;36:431–45.
[18] Fotsa RT, Woafo P. Chaos in a new bistable rotating electromechanical system, chaos. Solitons Fractals 2016;93:48–57.
[19] Jang JO, Jeon GJ. A parallel neuro-controller for DC motors containing nonlinear friction. Neurocomputing 2000;30:233–48.
[20] Lyshevski LE. Nonlinear control of mechatronic systems with permanent-magnet DC motors. Mechatronics 1999;9:539–52.